

# Multi-hit armour characterisation of metal-composite bi-layers

K. Karthikeyan, B.P. Russell\*, V.S. Deshpande and N.A. Fleck  
Department of Engineering, Cambridge University, U.K

\* Corresponding author (bpr23@cam.ac.uk)

## Abstract

The ballistic performance of equi-mass plates made from (i) stainless steel (SS); (ii) carbon fibre/epoxy (CF) laminate and (iii) a hybrid plate of both materials has been characterised for a spherical steel projectile. The hybrid plate was orientated with steel on the impact face (SSCF) and on the distal face (CFSS). The penetration velocity ( $V_{50}$ ) was highest for the SS plate and lowest for the CF plate. A series of double impact tests were performed, with an initial velocity  $V_I$  and a subsequent velocity  $V_{II}$  at the same impact site. An interaction diagram in  $(V_I, V_{II})$  space was constructed to delineate penetration from survival under both impacts. The degree of interaction between the two impact events was greater for the CFSS plate than for the SSCF plate, implying that the distal face has the major effect upon the degree of interaction.

*Keywords: composite, damage, ballistic loading, multi-impact, bi-layers*

## 1. Introduction

Composite materials are increasingly used in transportation and protection systems as they can give significant weight savings over their metallic counterparts. In a number of these applications there is a need for high impact resistance. For example, military vehicles are required to resist projectile impacts while in civilian aerospace applications the gas turbine (and airframe) needs to resist impacts from birds and other foreign objects. In most cases, the structure needs to be able to maintain its integrity under multiple impacts. The primary aim of this paper is to characterise the multi-impact ballistic performance of composite and metal/composite hybrid plates and to compare their performance with the reference case of a metallic plate of equal areal mass.

### 1.1 Ballistic damage characterisation

The residual strength of continuous fibre reinforced composite panels has been extensively investigated in the literature. A plethora of characterisation techniques assessing composite damage have been developed. All can be classified as either *visual techniques* or *residual performance tests*. Visual techniques include laser shearography [Hung 1982], X-ray tomography, thermography, digital image strain mapping, ultra-sound and both visual and electron microscopy. They are used to identify damage with a view to informing and validating computational modelling techniques. Residual performance tests are designed to ascertain the ability of a component to maintain function without necessarily developing an understanding of the mechanisms at play. Examples include post-impact compression tests (PICS) and tension after impact (TAI). [Cantwell and Morton 1991], and [Richardson and Wisheart 1996] have written reviews and detail these techniques for damage assessment. For example, [Kazemahvazi et al. 2010] assessed the residual strength of composite panels with the TAI technique. While most studies focus on damage characterisation after a single impact, [Appleby-Thomas et al. 2011] have recently investigated the damage mechanisms in carbon fibre composites subject to multiple impacts using both PICS and CT-scan techniques.

### 1.2 Hybridisation of materials

Polymer-matrix composites are increasingly used in light-weight transport due to their high specific strength and stiffness. However, their impact resistance is often inferior to their metallic counterparts. Recently, hybrid material systems, combining composite and metal, have been developed in order to combine high specific stiffness, strength and impact resistance. For example, Fibre Metal Laminates (FMLs) such as GLARE (Glass Laminate Aluminium Reinforced Epoxy) are finding application in the latest generation of commercial aircraft due to their superior performance under service and blast/impact loads [Vlot 1993; Young et al. 1994; Lambert 1995], when compared with equivalent mass metallic structures. The multi-impact performance of such hybrid panels has not been reported to-date.

### 1.3 Objectives of study

The objectives of this study are two-fold. First, this paper proposes a methodology to assess ballistic performance of plates under multi-hit. The focus here is restricted to two consecutive impacts at the same location although the scheme developed can be extended to more complex situations. Secondly, we use this methodology to assess the performance of metallic, composite and hybrid plates subject to projectile loadings.

## 2. Experimental protocol

Three types of clamped circular plates were impacted normally (zero obliquity) and centrally with spherical steel balls. The three plate types were (i) monolithic 304 stainless steel; (ii) 0–90° carbon fibre/epoxy laminate and (iii) a hybrid plate comprising a steel plate bonded

to a carbon fibre/epoxy laminate. All had an areal mass of approximately  $5.7 \text{ kg m}^{-2}$ . The aims of the experimental investigation were as follows.

- (i) To develop a methodology to characterise ballistic performance of plates subjected to two impacts at the same location.
- (ii) To compare the ballistic performance of the three plate types for both a single impact as well as two impacts at the same location.
- (iii) To determine the sensitivity of the ballistic performance of the hybrid plates to the orientation of the plate; i.e. whether the impacted face is the steel or composite face of the plate.

## 2.1 Materials and manufacture

Square plates measuring  $150 \text{ mm} \times 150 \text{ mm}$  were manufactured to the following specification:

- (i) *Monolithic steel plates*: Cold-rolled 304 stainless steel plates of thickness 0.70 mm were water jet cut from as-received stainless steel sheets of the same thickness.
- (ii) *Monolithic composite plates*: The composite plates comprised  $0-90^\circ$  laminates with IM7-12k carbon fibres embedded within a HexPly® 8552 resin. Alternating  $0^\circ$  and  $90^\circ$  plies (each of thickness 0.25mm) were stacked to construct a plate with lay-up  $[(0^\circ/90^\circ)_7/0^\circ]$ , overall thickness 3.75mm and density  $1570 \text{ kg m}^{-3}$ . Large composite plates were manufactured via a standard lay-up and autoclaving procedure, and cut to the requisite size with a diamond saw.
- (iii) *Hybrid plates*: The hybrid plates comprised a 0.3 mm cold-rolled stainless steel plate bonded to a 2 mm thick composite plate with lay-up  $[0^\circ/90^\circ]_4$ , i.e. 60% by mass composite. The hybrid plates were manufactured as follows. The cold-rolled steel and cured composites plates (manufactured from the same materials and using the same procedure as for the monolithic composite plates) were bonded together with a chemical cure epoxy resin system, Redux 810<sup>1</sup> as shown schematically in Fig. 1. First the bonding surfaces were cleaned thoroughly and then the epoxy applied to both surfaces. Both these surfaces were then bonded under a pressure of 22 kPa for a period of 5 hours. This procedure ensured a thin bond thickness and eliminated air gaps. The plates were allowed to cure for a further 120 hours to achieve full strength before testing. Note that the use of a room temperature chemically curing adhesive ensured that we minimised the build up of interfacial stresses due to the differences in thermal expansion coefficients between the two materials.

**Table 1** presents the geometric details of all the plates used in this study along with the designations by which each of these plates will be referred to subsequently. Note that the hybrid plates are used in two configurations: (i) SSCF where the stainless steel (SS) surface is the impacted face while the carbon fibre (CF) plate is the rear surface and (ii) CFSS where the CF plate is the impacted face.

## 2.2 Material properties

The quasi-static uniaxial compressive and tensile responses of the carbon fibre laminates with lay-up  $[(0^\circ/90^\circ)_7/0^\circ]$ , was measured at an applied nominal strain rate  $10^{-3} \text{ s}^{-1}$  using the

---

<sup>1</sup> Manufactured by Hexcel Composites.

procedure detailed in [Russell et al. 2008]. In brief, dogbone-shaped specimens were cut from the composite sheets. The tensile responses in the  $0-90^\circ$  and  $\pm 45^\circ$  orientation (where the angles refer to the angles between the fibre direction and the loading axis) were measured by friction gripping of these specimens and then conducting tensile tests in a screw-driven test machine. The applied load was measured via the load cell of the test machine and was used to define the applied stress while a  $0/90^\circ$  strain gauge rosette was used to measure the axial and transverse strain components. In order to perform compression tests that do not lead to premature failure by Euler buckling of the specimens, a sandwich column comprising an aluminium hexagonal honeycomb core and the face sheets made from the test composite material were constructed. The compression tests were also performed in the screw driven test machine with the loads and strain measured in a similar manner to that described for the tensile tests. Tensile tests on the 0.3 mm thick 304 stainless steel sheets were also conducted on dogbone-shaped specimens in a manner similar to the composite specimens. One key difference in the experimental methodology is that due to the larger strains in the stainless steel, a laser extensometer rather than strain gauges was used to measure strain in the tensile tests on the stainless steel.

The measured tensile responses of the  $0-90^\circ$  and  $\pm 45^\circ$  CFRP laminates is plotted in Fig. 2a. While the  $0-90^\circ$  is elastic-brittle with a tensile strength of about 1 GPa, the  $\pm 45^\circ$  has a non-linear response that can be approximated as elastic perfectly plastic with a yield strength of about 80 MPa and a tensile ductility of 5%. This difference is due to the fact that while the  $0-90^\circ$  laminate response is governed by the tensile response of the  $0^\circ$  carbon fibres the response of the  $\pm 45^\circ$  laminate is governed by the shear response of the matrix. The compressive strength of the laminate is approximately 630 MPa and set by the micro-buckling strength of the  $0^\circ$  plies. The 304 stainless steel has an elastic-plastic response with approximately linear work hardening after initial yield. It has a significantly higher ductility compared to the CFRP with a true necking strain of about 60% (Fig. 2b).

### 2.3 Ballistic measurement set-up and test methodology

A schematic of the experimental set-up is shown in Fig. 3. A gas-gun with a barrel length of 4.5 m and a bore of diameter 13 mm was used to accelerate steel spheres of diameter 12.7 mm and mass  $M = 8.3 \times 10^{-3}$  kg at velocities  $V_0$  ranging  $25 \text{ ms}^{-1}$  to  $210 \text{ ms}^{-1}$ . These projectiles impacted the test plates normally and centrally. A set of laser gates situated at the end of the barrel were used to measure the velocity of the projectile as it exits the barrel and prior to impact. The test plates were clamped between two annular steel plates of inner diameter 100 mm. Twelve equi-spaced holes of 6 mm diameter were drilled through the test plates on a pitch radius 62.5 mm, such that the specimens could be sandwiched between the clamping rings to ensure a clamped boundary condition. High speed photography was used to observe the impacted face of the plates during the experiments. A grid pattern was marked onto the face to clarify the deformation resultant from the impact. A Phantom V12 Camera<sup>2</sup> was used to visualise the dynamic deformation with an inter-frame time of  $15 \mu\text{s}$  and an exposure time of  $1 \mu\text{s}$ . In some cases the camera was used to view the impacted surface so as to be able to measure the rebound velocity of the projectile while in other cases the camera viewed the distal surface in order to visualise the dynamic deformation of the rear of the plate and the penetration of the projectile.

---

<sup>2</sup> Vision Research, 100 Dey Rd. Wayne, NJ 07470, USA

For each plate configuration, there exists a limiting projectile velocity  $V_L$  at which the plate is on the cusp of failure, i.e. a fractional increase in the impact velocity  $V_0$  will result in the penetration of the plate. This limiting velocity was determined to an accuracy of  $1-5 \text{ ms}^{-1}$  by performing a series of tests at impact velocities  $V_0$  in the vicinity of  $V_L$ . In the case of the stainless steel plates, the failure/penetration of the plates was clearly seen after the test. However, in the case of the composite specimens, there was a large degree of spring-back resulting in closure of the hole created by the penetrated projectile. This could result in an erroneous conclusion that the plate had survived the impact event, if the judgement was made by inspection of the plate after the test. Further, the high degree of spallation from the back of the composite plates also made it difficult to judge via high speed photography whether the projectile had penetrated the composite plates. Thus, a corrugated cardboard “witness” plate was placed 20 cm behind the composite plate: penetration of this witness plate by the projectile is clearly seen after the impact event and was used to confirm the penetration of the composite plates.

#### 2.4 Ballistic characterisation technique

The ballistic performance of the targets is characterised via two metrics in this study:

- (i) The *ballistic limit*  $V_L$ . It denotes the critical velocity at which a given projectile just penetrates the target, and is often referred to as  $V_{50}$  in the literature.
- (ii) A *limit surface* in velocity space, to delineate penetration from survival due to an initial velocity  $V_I$  and a subsequent velocity  $V_{II}$ . Both impacts on the plate occur normally and centrally. A series of double impact tests, with an initial velocity  $V_I$  and a subsequent velocity  $V_{II}$  at the same impact site allow for the construction of an interaction diagram in  $(V_I, V_{II})$  space.

The limit surface in  $V_I - V_{II}$  space is depicted in **Fig. 4a**. The interpretation of this limit surface is as follows. For any combination of  $V_I$  and  $V_{II}$  that lies inside this limit surface, the projectile does not penetrate the target after the second impact while the target is penetrated if the combination of these velocities lies on or outside this limit surface. By definition, when  $V_I = V_L$ ,  $V_{II} = 0$  and conversely  $V_{II} = V_L$  when  $V_I = 0$ . The form of the limit surface at intermediate values of  $V_I$  and  $V_{II}$  depends strongly upon the material properties of the target. For example, we anticipate that an elastic-brittle target will undergo negligible damage for impacts at a velocity less than  $V_L$  resulting in no interaction between  $V_I$  and  $V_{II}$ . Thus, the limit surface for an elastic-brittle target is expected to be square such that  $\max(V_I, V_{II}) = V_L$  as depicted in **Fig. 4b**. On the other hand, a more ductile target that undergoes progressive damage will have significant interaction between  $V_I$  and  $V_{II}$  resulting in a limit surface that lies inside the square limit surface of the elastic-brittle target; see **Fig. 4b**. In this study we shall determine the forms of these limit surfaces of the 4 plate configurations detailed in Section 3.

In addition to the ballistic limit surfaces in  $V_I - V_{II}$  space we will also report the performance of the plates in terms of two additional metrics:

- (i) The *rebound velocity*  $V_R$ : The rebound velocity of the steel ball for first impacts at a velocity  $V_I < V_L$  was measured via high speed photography. We report this rebound

velocity in terms of a co-efficient of restitution  $e \equiv -V_R/V_I$ , where  $e$  is a positive number as  $V_R$  and  $V_I$  have opposite signs.

- (ii) The *equi-velocity ballistic limit*  $V_{2L}$ : The limit surfaces in  $V_I - V_{II}$  space provide a detailed view of the double impact ballistic performance of the plates. It is useful to define a simple scalar measure that quantifies this double hit ballistic performance. The equi-velocity ballistic limit  $V_{2L}$  is the penetration velocity along the trajectory  $V_I = V_{II}$ ; see Fig. 4a. We report it in the normalised form  $\bar{V}_{2L} \equiv V_{2L}/V_L$  in order to quantify the reduction in the penetration velocity over the single hit ballistic limit  $V_L$ .

### 3. Ballistic performance of plates

The measured ballistic limit surfaces of the four types of plates investigated here are plotted in Fig. 5 with the first impact velocity  $V_I$  plotted in the  $x$ -axis and the second impact velocity  $V_{II}$  plotted on the  $y$ -axis. Data points corresponding to no penetration (marked by circles) and penetration (marked by crosses) are plotted in Fig. 5 while the ballistic limit boundary in  $V_I - V_{II}$  is space sketched by interpolating between the circles and the crosses. Figure 6 shows these same limit surfaces plotted together. We shall first describe the key measurements and then proceed to discuss the observed penetration mechanisms.

*Single hit performance:* For the given areal mass and projectile the ballistic limit  $V_L$  or  $V_{50}$  increases in the following order: (i) Carbon fibre plates (CF); (ii) hybrid plate with steel front (SSCF); (iii) hybrid plate with carbon fibre front (CFSS) and (iv) monolithic steel plate (SS); see Fig. 7.

*The ballistic limit surfaces:* The measured limit surfaces in Fig. 6a shows the comparative performance of all plates. The CF plate and both hybrid plates lie nested within the no penetration region of the SS plate. The hybrid plates display an interesting regime where the multi-hit performance of the SSCF give superior performance where  $V_I \approx V_{II}$ , and the CFSS plate superior at the extremes where  $V_I = V_{II}$  and  $V_{II} = V_I$ . The normalised limit surfaces in Fig. 6b indicate that the ballistic limits of the monolithic steel (SS) and carbon fronted hybrid plate (CFSS) degrades due to a first impact at a velocity  $\bar{V}_I < 1$  with the measured limit surface lying well within the ‘‘upper bound limit surface’’ described by  $\max(\bar{V}_I, \bar{V}_{II}) = 1$  and sketched by the dashed lines in Fig. 6b. On the other hand, the ballistic limit the carbon fibre plates (CF) and the steel front hybrid plates (SSCF) indicate that there is little interaction between the two impacts for these plates with the measured limit surfaces are close to the ‘‘upper bound’’. A lower limit - the linear interaction dashed line - is the maximum interaction of the two impacts assuming that the ballistic limit surface is convex.

*The equi-velocity ballistic limit:* The normalised equi-velocity ballistic limit  $\bar{V}_{2L}$  for the four plates investigated here are included in the bar chart in Fig. 7. Both the SS and CFSS plates have approximately a 40% reduction in their penetration velocities due to the first impact with  $\bar{V}_{2L} = 0.62$ . The reductions in the penetration velocities of the SSCF and CF plates is much less with  $\bar{V}_{2L} = 0.92$  and 0.8, respectively.

#### 3.1 Discussion on the penetration mechanisms

Photographs of the front and back surfaces of the penetrated plates are included in Fig. 8 for the SS and CF plates and in Fig. 9 for the CFSS and SSCF plates. These failed specimens

were penetrated after two impacts such that  $V_I = V_{II} = V_{2L}$ . Penetration of the monolithic steel plate occurs by ductile tearing around periphery of a circle whose diameter is approximately equal to the diameter of the projectile as seen in Figs. 8a and 8b. By contrast, the carbon fibre plate fails by fibre breakage of both the  $0^\circ$  and  $90^\circ$  fibres resulting in the square holes in seen Fig. 8c. Also, a strip of a single ply delaminates and is removed by the exiting projectile on the rear surface of the CF plate; see Fig. 8d. Clearly, the failure mechanism of the steel plate is ductile while the carbon fibre plate fails in a quasi-brittle mode.

In order to quantify the degree of inelasticity involved in the impact of the steel projectile against these plates we plot in Fig. 10 the effective co-efficient of restitution  $e$  as a function of the normalised impact velocity  $\bar{V}_I \equiv V_I / V_L$ . The rebound of the projectile off the composite plate is shown via a series of high speed photographs in Fig. 10a, for an impact velocity  $\bar{V}_I = 0.77$ . Time  $t = 0$  in these images corresponds to the instant of impact and hence we have shown images with both negative  $t$  (i.e. before impact with the projectile approaching the plate) and positive  $t$  corresponding to the time when the projectile has rebounded off the plate. The measured co-efficient of restitution plotted in Fig. 10b decreases from approximately 0.25 to less than 0.1 for the steel plate as the impact velocity increases from about  $\bar{V}_I = 0.1$  to the ballistic limit, i.e. the impacts can be viewed as significantly inelastic. By contrast,  $e \approx 0.5$  at low values of  $\bar{V}_I$  for the carbon fibre plates but decreases as  $V_I$  approaches the ballistic limit when we anticipate significant inelastic processes to occur in the impacted carbon fibre plate. We note in passing that the hardened steel projectiles (which are ball bearings) undergo negligible plastic deformation in any of the impacts investigated here. Thus,  $e$  can be directly related to the energy absorbed  $\Delta E$  by the target plate via the relation

$$\Delta E = \frac{1}{2} M V_I^2 (1 - e^2), \quad (3.1)$$

where  $M$  is the mass the projectile.

Photographs of the failed SSCF and CFSS hybrid plates are shown in Fig. 9. There is clear ductile deformation of the rear steel plate with brittle failure of the front carbon plate for the CFSS plate as seen in Figs. 9c and 9d, respectively. However, in the case of the SSCF plate the stiff rear carbon plate prevents ductile deformation of the front steel plate. This results in a plugging type failure of the front steel plate followed by the usual brittle failure of the carbon rear plate. We thus anticipate that overall deformation/failure processes in the SSCF plates involve significantly less inelastic processes compared to the CFSS plates. This is borne out further by two observations:

- (i) The co-efficient of restitution plotted in Fig. 10b is higher for the SSCF plates compared to the CFSS plates.
- (ii) The ballistic limit surface of the SSCF plate (Fig. 5) shows that there is little interaction between  $V_I$  and  $V_{II}$  resulting in a failure surface that is well approximated by ‘‘upper bound’’  $\max(V_I, V_{II}) = V_L$ . By contrast, in the CFSS plates, the initial impact results in a significant reduction in the ballistic limit for the second impact and the ballistic failure surface lies well inside the upper bound; see Fig. 5d.

### 3. Concluding remarks

The ballistic performance of three types of plates, all with the same areal mass was investigated for both single and two impacts at the same location by a steel ball bearing of diameter 12.7 mm. The three types of plates were (i) monolithic stainless steel; (ii) monolithic carbon fibre/epoxy (CFRP) laminates with equal number of  $0^\circ$  and  $90^\circ$  plies and (iii) a hybrid laminate plate comprising a stainless steel plate glued on to a  $0^\circ/90^\circ$  carbon fibre plate. This hybrid plate had 60% by mass CFRP. The hybrid plates were tested in two orientations: the steel facing on the impact side and vice versa.

The single impact ballistic resistance was characterised in terms of the usual metric, viz. the  $V_{50}$  defined as the limiting projectile velocity at which the plate is just penetrated. In terms of the  $V_{50}$ , the ballistic limit is the highest for the stainless steel plate, followed by the hybrid plate with the CFRP on the impacted side. The ballistic limit of the same hybrid plate is slightly lower when the stainless steel is on the impacted side. Monolithic CFRP has the lowest ballistic limit. The double impact ballistic performance was characterised by measuring the ballistic limit surfaces that give the limiting velocity  $V_{II}$  required to penetrate the plate after an initial impact at a velocity  $V_I < V_{50}$ . While the steel plate has the highest ballistic limit, it undergoes significant damage after an initial impact which means that the second hit ballistic limit  $V_{II}$  decreases significantly with increasing  $V_I$ . The same is true for the hybrid plate with the steel on the rear face as the steel delaminates from the CFRP and responds independently. By contrast, the ballistic performance of the monolithic CFRP plate and the hybrid plate with steel on the impacted face is not significantly affected by the initial impact as the CFRP responds in an elastic-brittle manner, i.e. it either breaks and allows the projectile to penetrate or responds elastically which results in the projectile rebounding off the plate.

This study has demonstrated that while the ballistic performance of CFRP plates is lower than that of a steel plate on an equal mass basis, CFRP and CFRP hybrid plates might be considered for ballistic applications especially if the application requires the plate to withstand multiple impacts. The study has also demonstrated the sensitivity of the ballistic performance to the orientation of the hybrid plates, viz. while the ballistic limit surface of the hybrid plate with CFRP facing the impact is qualitatively similar to the steel plate, the hybrid plate with steel on the impacted surface behaves more like the monolithic CFRP plate.

## References

- [Appleby-Thomas et al. 2011] G. J. Appleby-Thomas, P. J. Hazell, and G. Dahini, “On the response of two commercially-important CFRP structures to multiple ice impacts”, *Composite Structures*, **93**:10 (2011), 2619–2627.
- [Cantwell and Morton 1991] W. Cantwell, and J. Morton, “The impact resistance of composite materials — a review”, *Composites*, **22**:5 (1991), 347–362.
- [Hung 1982] Y. Hung, “Shearography - A New Optical Method For Strain-Measurement And Non-Destructive Testing”, *Optical Engineering*, **21**:3 (1982), 391–395.
- [Kazemahvazi et al. 2010] Kazemahvazi, S., Kiele, J., & Zenkert, D.. Tensile strength of UD-composite laminates with multiple holes. *Composites Science and Technology*, **70**:8 (2010), 1280–1287.
- [Lambert 1995] M. Lambert, “Shielding against space debris. A comparison between different shields: The effect of materials on their performances”, *International Journal of Impact Engineering*, **17**:4-6 (1995), 477–485.
- [Richardson and Wisheart 1996] M. Richardson, and M. Wisheart, “Review of low-velocity impact properties of composite materials”, *Composites Part A: Applied Science and Manufacturing*, **27**:12 (1996), 1123–1131.
- [Russell et al. 2008] B. P. Russell, V. S. Deshpande and H. N. G. Wadley, “Quasistatic deformation and failure modes of composite square honeycombs”, *Journal of Mechanics of Materials and Structures*, **3**:7 (2008), 1315–1340.
- [Vlot 1993] A. Vlot, “Impact properties of Fibre Metal Laminates”, *Composites Engineering*, **3**:10 (1993), 911–927.
- [Young et al. 1994] J. B. Young, J. G. N. Landry, and V. N. Cavoulacos, “Crack growth and residual strength characteristics of two grades of glass-reinforced aluminium ‘Glare’”, *Composite Structures*, **27**:4 (1994), 457–469.

## Acknowledgements

The authors are grateful for financial support from the US Office of Naval Research (contract N62909-10-1-7122). Dr B. P. Russell was supported by a Ministry of Defence / Royal Academy of Engineering Research Fellowship.

## Figure Captions

Fig. 1: Manufacturing route for the hybrid bi-layer plates: (a) metal plates are cut to the required size by waterjet and the composite plates cut by a diamond saw; (b) acetone is used to clean the metal surfaces before Redux 810 adhesive is applied to both the metal and composite surfaces; (c) over the initial 5 hours of the cure cycle, the specimen is held under pressure after which (d) the adhesive is allowed a further 5 days to harden to full strength.

Fig. 2: (a) The measured tensile and compressive stress versus strain responses of the materials used in the plate construction. (b) The full tensile stress versus strain response of the stainless steel beyond the onset of necking.

Fig. 3: (a) Plan view of the plate test fixture showing the plate geometry and the clamping arrangement. (b) A side view of the test set-up showing the showing end of the barrel of the gas gun and the clamped plate. All dimensions are in mm.

Fig. 4: (a) Sketch illustrating the measurement of the ballistic limit surface in  $V_I - V_{II}$  space. For a given  $V_I < V_L$  tests are done for increasing values of  $V_{II}$  to locate the limiting penetration velocity as indicated by the circles and crosses. The definition of the equi-velocity penetration limit  $V_{2L}$  is also included. (b) A sketch of the upper bound ballistic limit surface defined by  $\max(V_I, V_{II}) = V_L$  for an elastic-brittle material. An illustrative limit surface for a more ductile material is also included.

Fig. 5: The measured ballistic limit surfaces in  $V_I - V_{II}$  space for (a) monolithic stainless steel (SS), (b) monolithic carbon fibre/epoxy (CF), (c) steel fronted hybrid (SSCF), and (d) composite fronted hybrid (CFSS). The crosses mark experiments corresponding to penetration while the circles are experiments where the plates survived. The “upper-bound” limit surface is sketched in via a dashed line in each case.

Fig. 6: A bar chart plotting the measured ballistic limit  $V_L$  or  $V_{50}$  as well as the normalised equi-velocity ballistic limit  $\bar{V}_{2L}$  for the four plate configurations investigated here.

Fig. 7: Post-test images of the steel (SS) and carbon fibre/epoxy (CF) plates impacted at velocities  $V_I = V_{II} = V_{2L}$ . The front and rear faces of the SS plate are shown in (a) and (b) while the (c) and (d) show images of the front and rear, respectively of the CF plate.

Fig. 8: Post-test images of the steel fronted hybrid (SSCF) and carbon fibre/epoxy front hybrid (CFSS) plates impacted at velocities  $V_I = V_{II} = V_{2L}$ . The front and rear faces of the SSCF plate are shown in (a) and (b) while the (c) and (d) show images of the front and rear, respectively of the CFSS plate.

Fig. 9: (a) High-speed photographs showing the rebound of the projectile impacting the carbon fibre/epoxy (CF) plate at  $\bar{V}_I = 0.77$ . In these images time  $t = 0$  corresponds to the instant of impact. (b) The measured effective co-efficient of restitution  $e$  of the projectile as a function of the normalised impact velocity  $\bar{V}_I$  for the four plate configurations investigated here.

## Tables

Table 1: Materials and geometry of the four plate configurations investigated here.

<b>Designation</b>	<b>Thickness, <math>t</math> (mm)</b>	<b>Impact Face</b>	<b>Distal Face</b>	<b>Areal mass (kgm<sup>-2</sup>)</b>
SS	0.71	304 Stainless steel		5.55
CF	3.75	CF/epoxy [(0°/90°) <sub>7</sub> /0°]		5.85
SSCF	0.3 / 2	304 Stainless steel	CF/epoxy [0°/90°] <sub>4</sub>	5.65*
CFSS	2 / 0.3	CF/epoxy [0°/90°] <sub>4</sub>	304 Stainless steel	5.65*

\*Inclusive of adhesive layer (0.19 kg m<sup>-2</sup>)

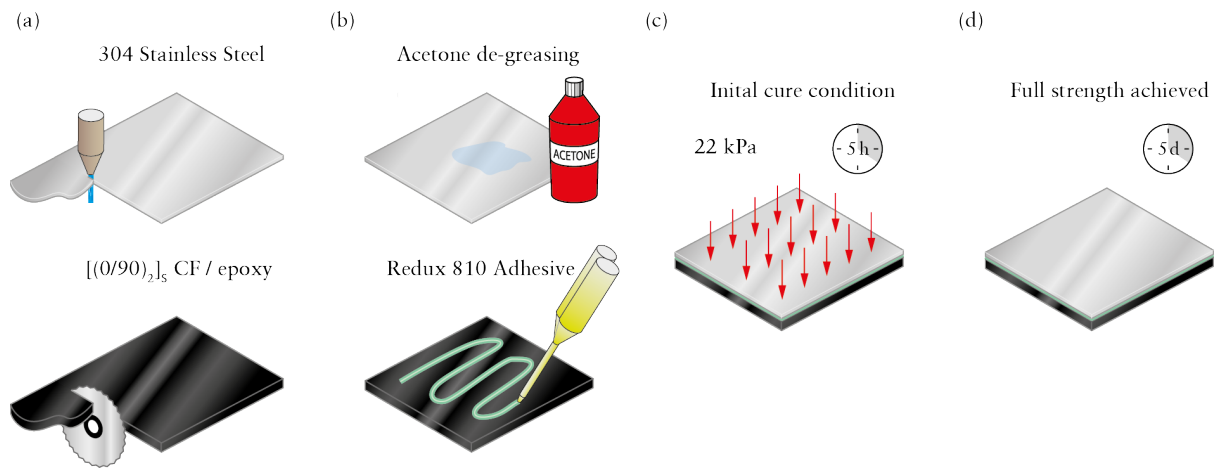


Fig. 1: Manufacturing route for the hybrid bi-layer plates: (a) metal plates are cut to the required size by waterjet and the composite plates cut by a diamond saw; (b) acetone is used to clean the metal surfaces before Redux 810 adhesive is applied to both the metal and composite surfaces; (c) over the initial 5 hours of the cure cycle, the specimen is held under pressure after which (d) the adhesive is allowed a further 5 days to harden to full strength.

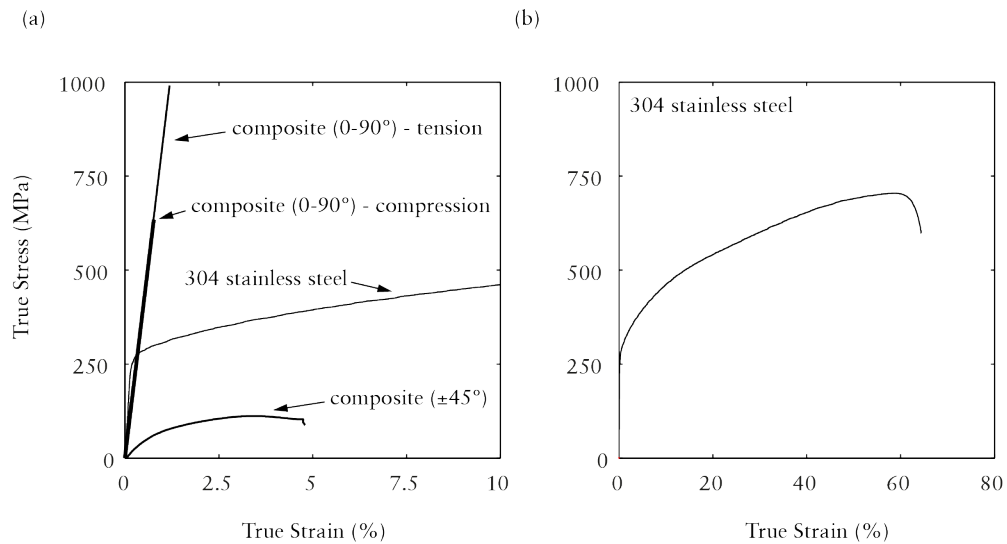


Fig. 2: (a) The measured tensile and compressive stress versus strain responses of the materials used in the plate construction. (b) The full tensile stress versus strain response of the stainless steel beyond the onset of necking.

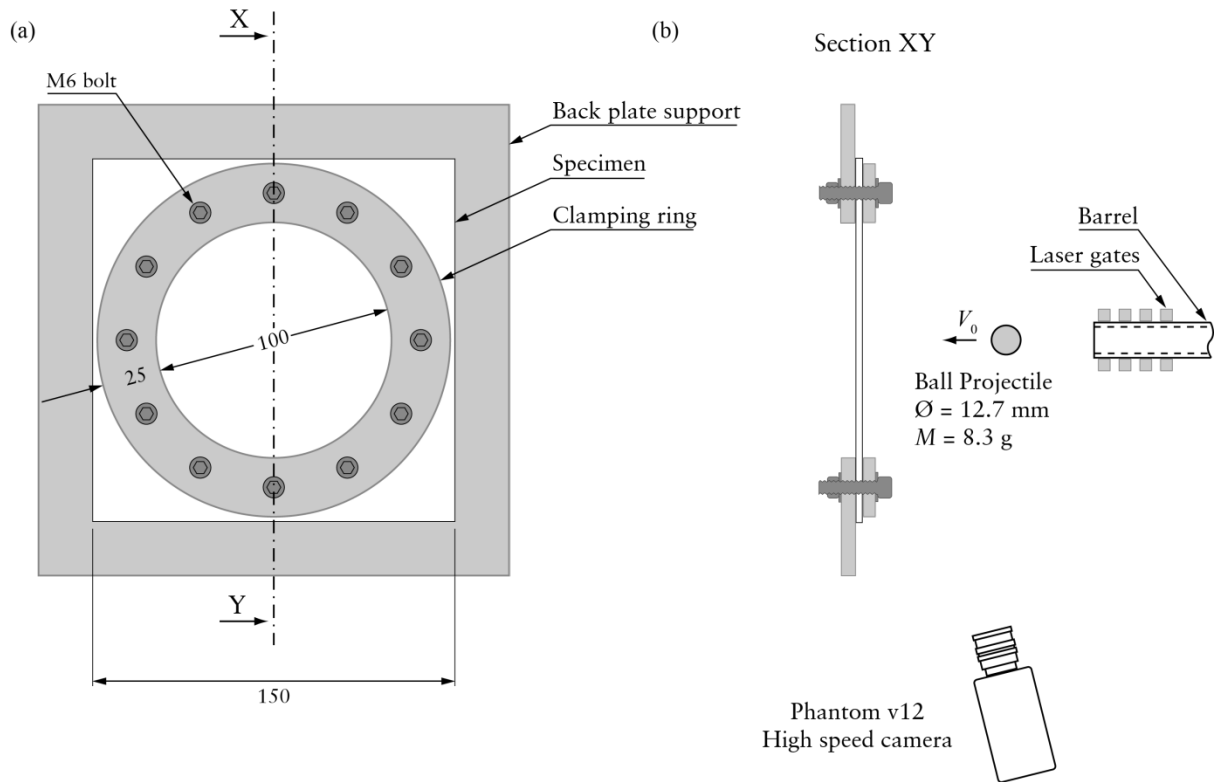


Fig. 3: (a) Plan view of the plate test fixture showing the plate geometry and the clamping arrangement. (b) A side view of the test set-up showing the showing end of the barrel of the gas gun and the clamped plate. All dimensions are in mm.

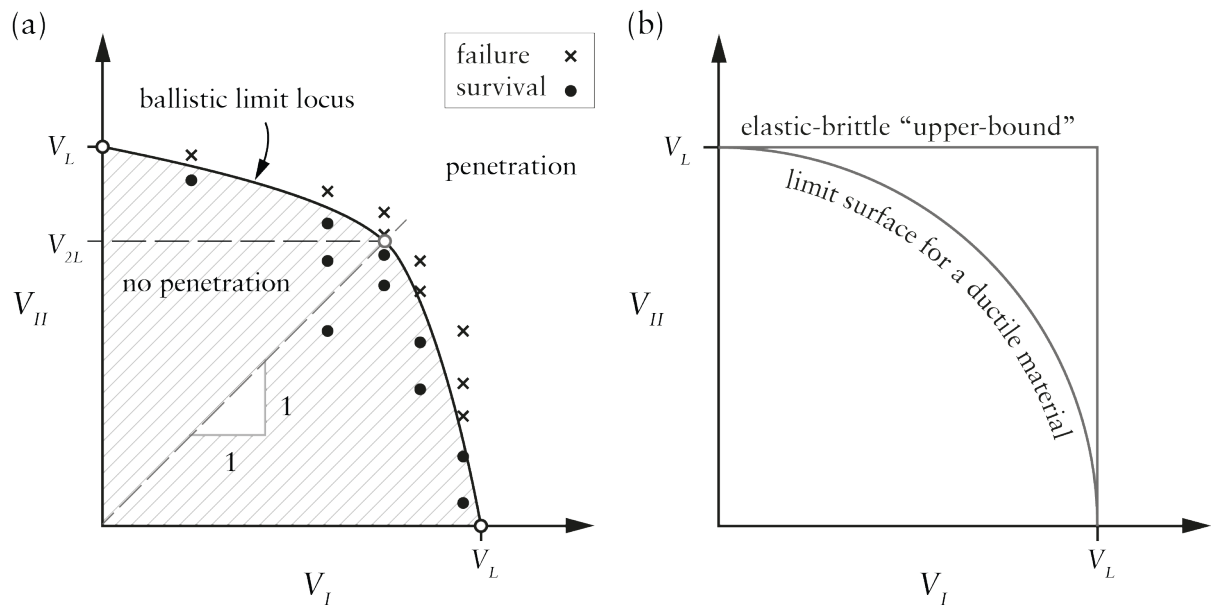


Fig. 4: (a) Sketch illustrating the measurement of the ballistic limit surface in  $V_I - V_{II}$  space. For a given  $V_I < V_L$  tests are done for increasing values of  $V_{II}$  to locate the limiting penetration velocity as indicated by the circles and crosses. The definition of the equi-velocity penetration limit  $V_{2L}$  is also included. (b) A sketch of the upper bound ballistic limit surface defined by  $\max(V_I, V_{II}) = V_L$  for an elastic-brittle material. An illustrative limit surface for a more ductile material is also included.

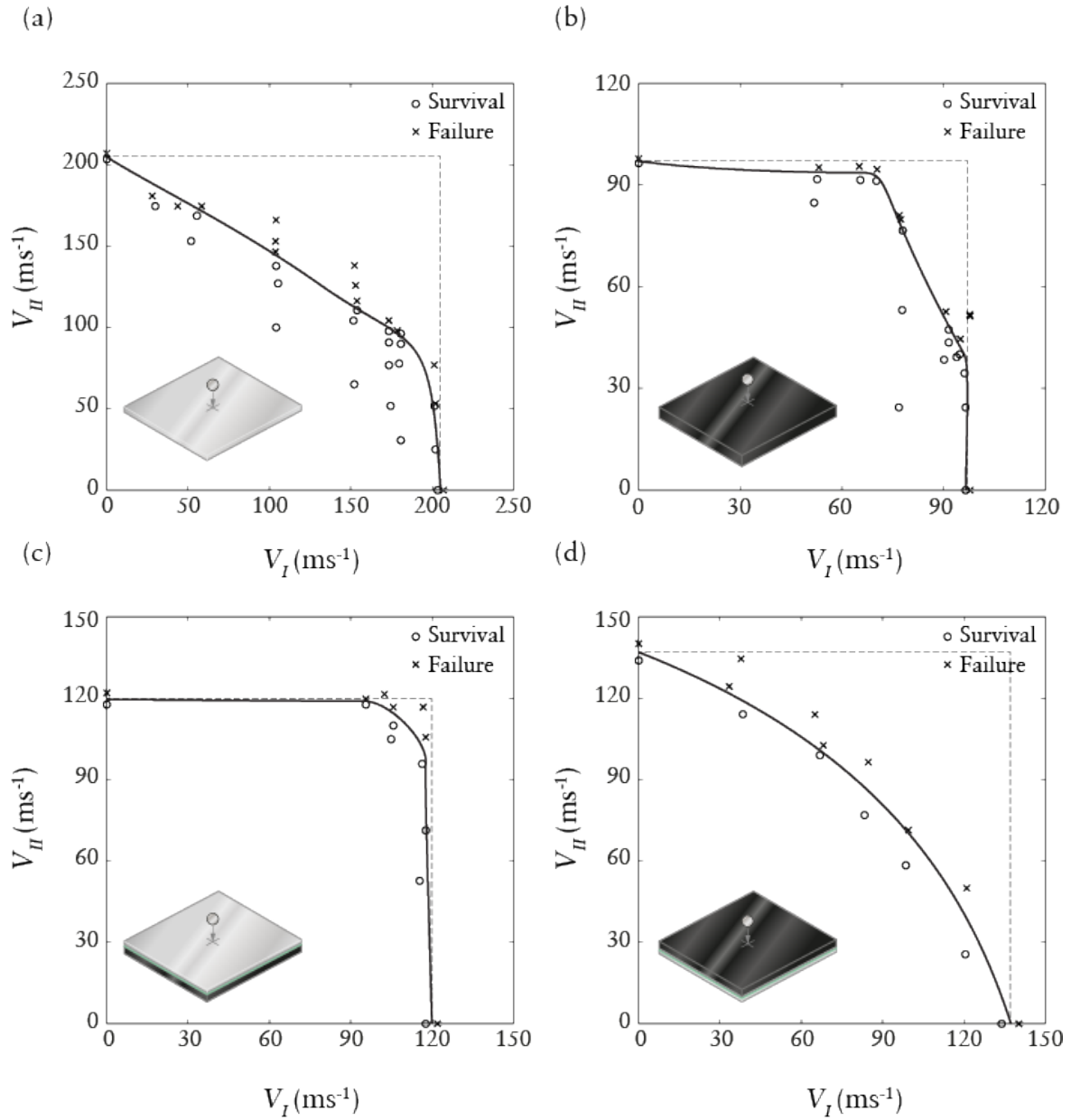


Fig. 5: The measured ballistic limit surfaces in  $V_I - V_{II}$  space for (a) monolithic stainless steel (SS), (b) monolithic carbon fibre/epoxy (CF), (c) steel fronted hybrid (SSCF), and (d) composite fronted hybrid (CFSS). The crosses mark experiments corresponding to penetration while the circles are experiments where the plates survived. The “upper-bound” limit surface is sketched in via a dashed line in each case.

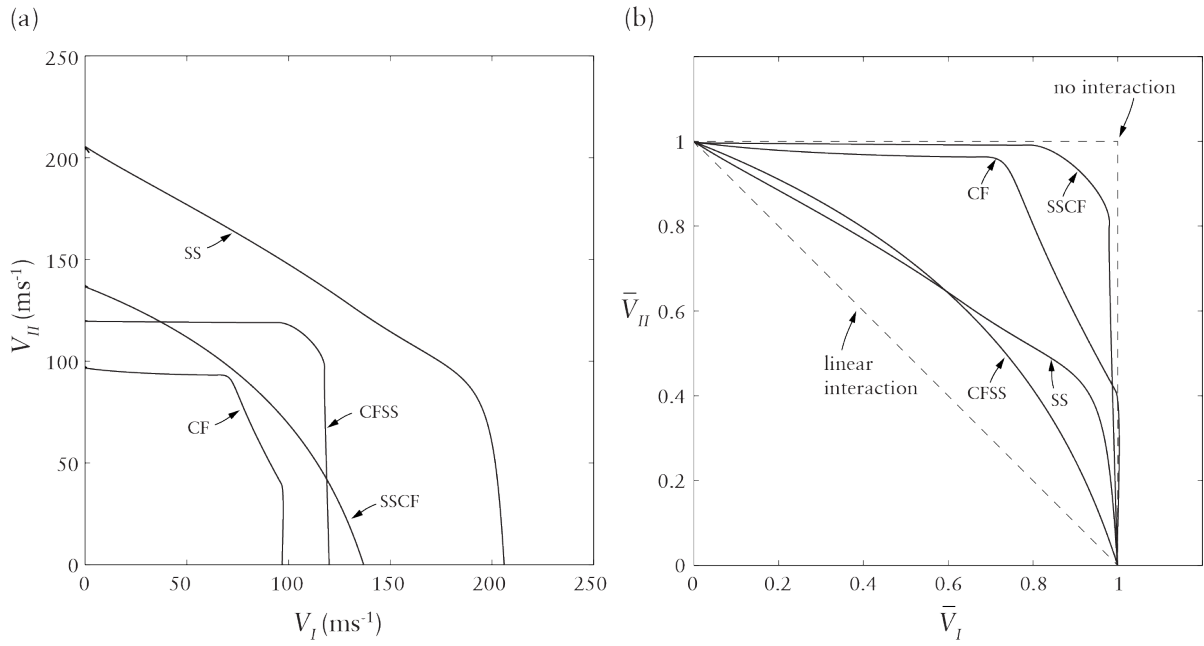


Fig. 6: Ballistic limit surfaces for all plates in (a)  $V_I - V_{II}$  space and (b)  $\bar{V}_I - \bar{V}_{II}$  space.

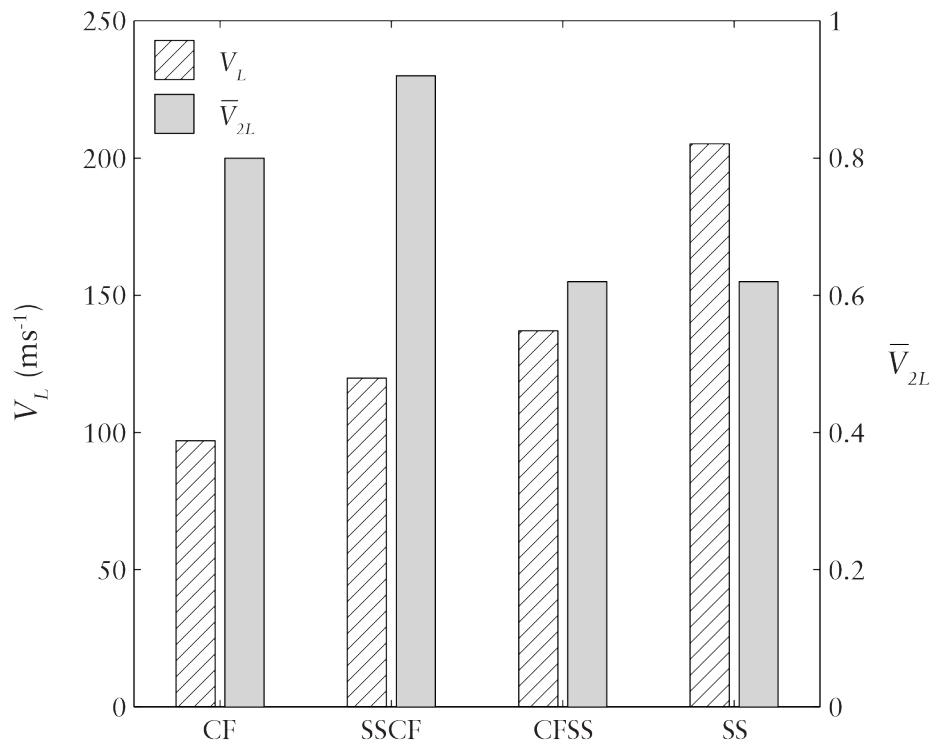


Fig. 7: A bar chart plotting the measured ballistic limit  $V_L$  or  $V_{50}$  as well as the normalised equi-velocity ballistic limit  $\bar{V}_{2L}$  for the four plate configurations investigated here.

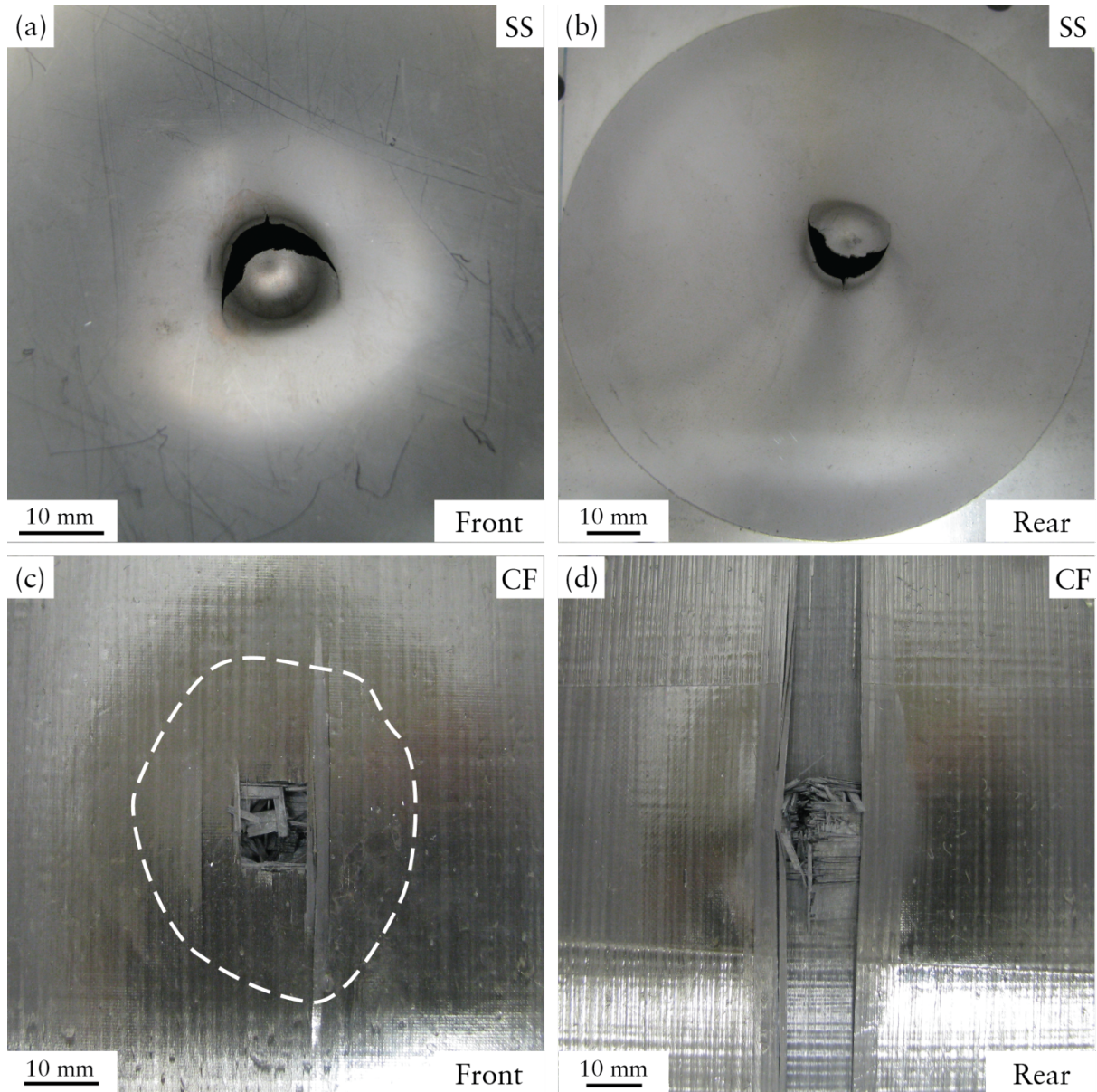


Fig. 8: Post-test images of the steel (SS) and carbon fibre/epoxy (CF) plates impacted at velocities  $V_I = V_{II} = V_{2L}$ . The front and rear faces of the SS plate are shown in (a) and (b) while the (c) and (d) show images of the front and rear, respectively of the CF plate.

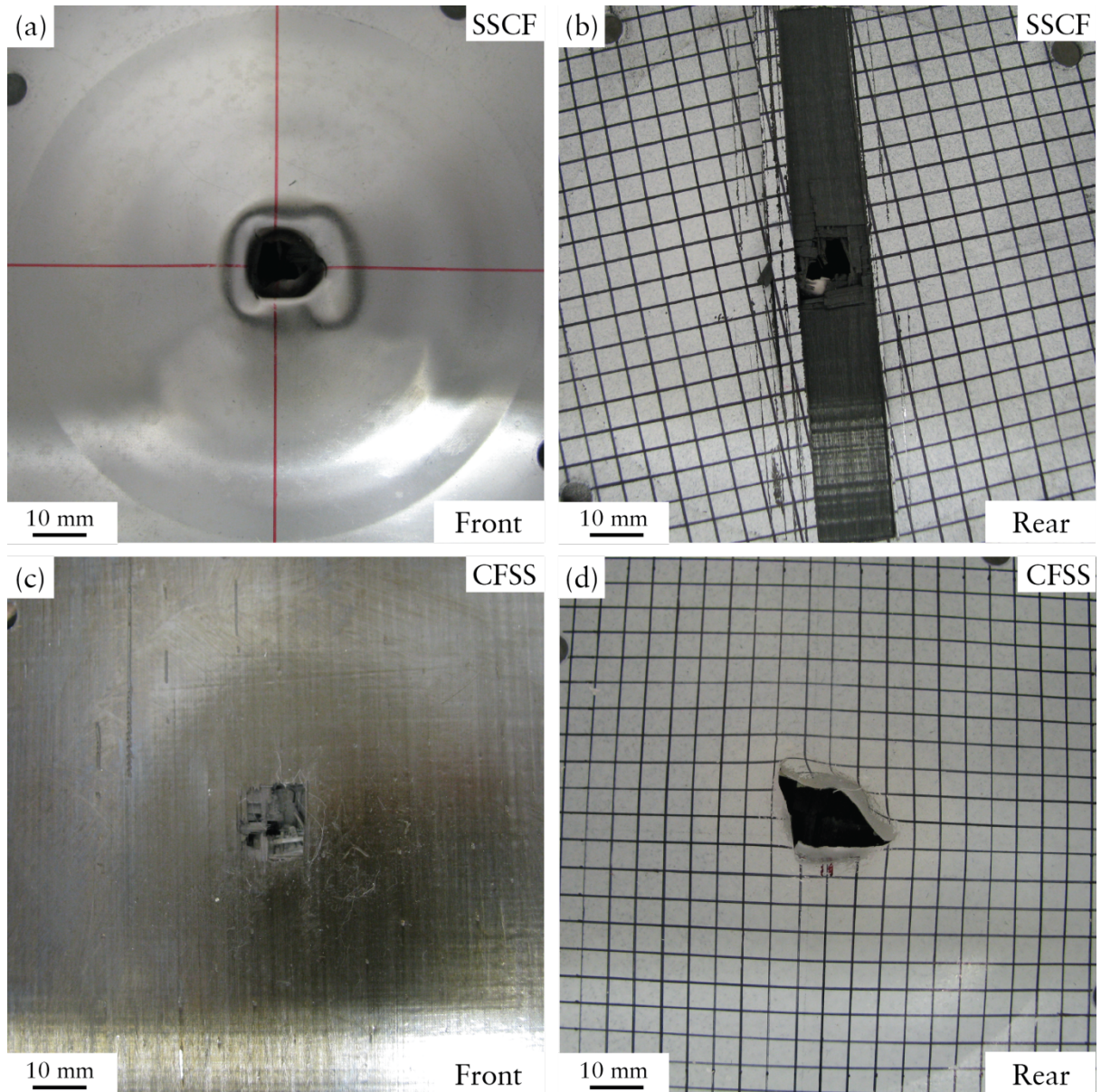
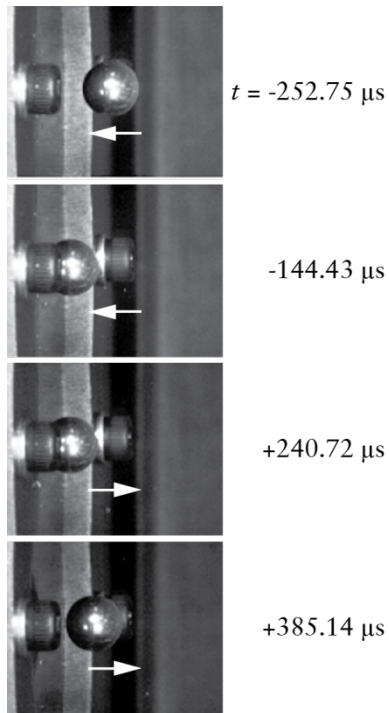


Fig. 9: Post-test images of the steel fronted hybrid (SSCF) and carbon fibre/epoxy front hybrid (CFSS) plates impacted at velocities  $V_I = V_{II} = V_{2L}$ . The front and rear faces of the SSCF plate are shown in (a) and (b) while the (c) and (d) show images of the front and rear, respectively of the CFSS plate.

(a)



(b)

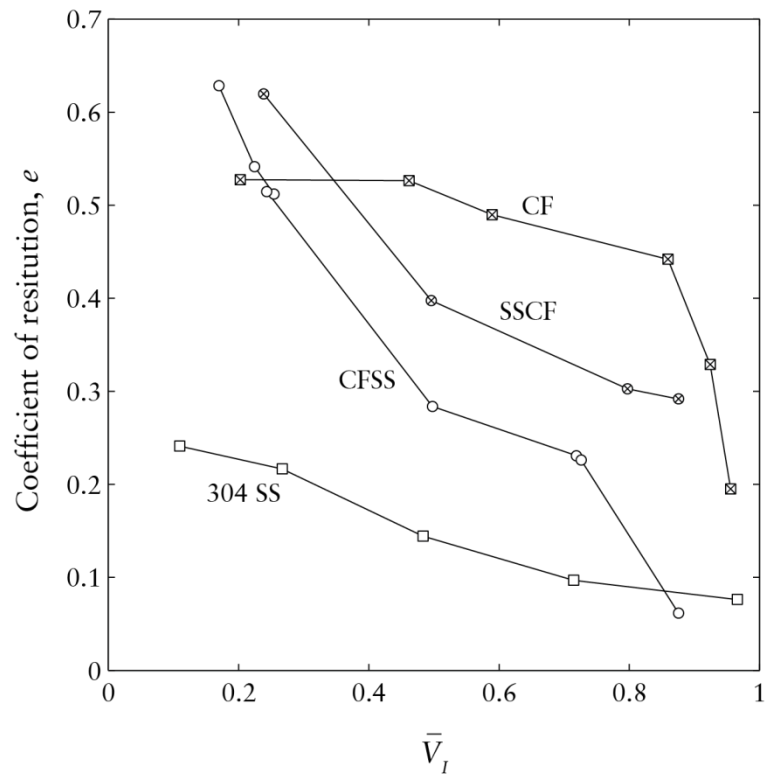


Fig. 10: (a) High-speed photographs showing the rebound of the projectile impacting the carbon fibre/epoxy (CF) plate at  $\bar{V}_I = 0.77$ . In these images time  $t = 0$  corresponds to the instant of impact. (b) The measured effective co-efficient of restitution  $e$  of the projectile as a function of the normalised impact velocity  $\bar{V}_I$  for the four plate configurations investigated here.